

Single-Photon Avalanche Diode Imagers Applied to Near-Infrared Imaging

Juan Mata Pavia, Martin Wolf, and Edoardo Charbon, *Senior Member, IEEE*

Abstract—Single-photon avalanche diodes (SPADs) can be integrated into large pixel arrays. The aim of this paper is to present a view on how these imagers change the paradigm of wide-field near-infrared imaging (NIRI). Thanks to the large number of pixels that they offer and to their advanced time-resolved measurement capabilities, new approaches in the image reconstruction can be applied. A SPAD imager was integrated in a NIRI setup to demonstrate how it can improve spatial resolution in reconstructed images. The SPAD imager has a time resolution of 97 ps and a picosecond laser source with an average output power of 3 mW was employed. The large amount of data produced by this new setup could not directly be analyzed with state-of-the-art image reconstruction algorithms. Therefore a new theoretical framework was developed. Simulations show that millimetric resolution is achievable with this setup. Experimental results have demonstrated that a resolution of at least 5 mm is possible with the current setup. A discussion about how different characteristics of the SPAD imagers affect the NIRI measurements is presented and possible future improvements are introduced.

Index Terms—Inverse problems, near-infrared imaging (NIRI), single-photon detector, time-resolved imaging.

I. INTRODUCTION

NEAR-infrared imaging (NIRI) is a relatively novel method that employs near-infrared light from 650 to 950 nm approximately to image biological tissue up to a depth of a few centimeters. When near-infrared light (NIR), travels through most biological soft tissue, it undergoes 5 to 20 scattering events per millimeter depending on the tissue. This process creates diffusive light waves that can be modeled by the diffusion equation. The main absorbers in human tissue in the NIR range are oxy- and deoxyhemoglobin (O_2Hb and HHb), although other substances such as water and lipid also absorb light [1]. By measuring the spectra of the light that is backscattered to the tissue's surface, it is possible to calculate the concentration of

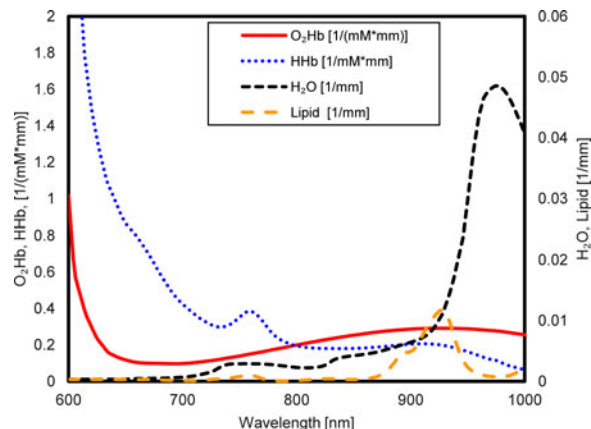


Fig. 1. Absorption spectra for O_2Hb , HHb , water, and lipid, the main absorbers in tissue in the near-infrared region.

the different absorbers in the tissue. Fig. 1 shows the absorption spectra for the main absorbers in human soft biological tissue.

By positioning light sources on the surface of the tissue and measuring the backscattered light at different locations, one can perform tomographic reconstructions of the different absorbers. These image reconstructions from NIRI data require primarily the definition of a model for the propagation of light in highly scattering media. Several authors have proposed a variety of models with different levels of computational complexity such as perturbation models [1], finite element methods [2], [3] or Monte Carlo methods [4]. Once the so-called forward model is established, an inverse problem is formulated using this model in which the optical properties of the object under reconstruction are obtained from the measurements at its surface [5]. Due to the scattering and absorbing characteristics of tissue, the problem is ill-posed by nature; this is not the case in other tomographic methods such as magnetic resonance imaging or computerized tomography. In NIRI there is always unrecoverable information encoded in light that was absorbed in the tissue. In most of the cases, the inverse problem will be underdetermined as well, because the amount of reconstructed voxels is frequently much higher than the measured information.

In an attempt to recover most of the backscattered light from the tissue and to reduce interferences from ambient light, NIRI devices have traditionally employed point sources and detectors. Such optical probes were directly attached to the surface of the tissue. This has limited the scalability of NIRI devices, making it impossible to construct systems with more than a few dozens of sources and detectors. It is thus desirable to increase the number of sources and detectors to obtain more information in order to reduce the ill-posed nature of the reconstruction problem.

Manuscript received February 1, 2014; revised March 20, 2014; accepted March 24, 2014. This work was partly supported by the KFSP Tumor Oxygenation and the KFSP Molecular Imaging of the University of Zurich, and by the National Competence Center for Biomedical Imaging.

J. Mata Pavia is with the Quantum Architecture Group, Ecole Polytechnique Federale de Lausanne, 1015 Lausanne, Switzerland and also with the Biomedical Optics Research Laboratory, Division of Neonatology, University Hospital Zurich, 8091 Zurich, Switzerland (e-mail: juan.matapavia@epfl.ch).

M. Wolf is with the Biomedical Optics Research Laboratory, Division of Neonatology, University Hospital Zurich, 8091 Zurich, Switzerland (e-mail: martin.wolf@usz.ch).

E. Charbon is with the Quantum Architecture Group, Ecole Polytechnique Federale de Lausanne, 1015 Lausanne, Switzerland and with TU Delft, 2628CD Delft, The Netherlands (e-mail: e.charbon@tudelft.nl).

Color versions of one or more of the figures in this paper are available online at <http://ieeexplore.ieee.org>.

Digital Object Identifier 10.1109/JSTQE.2014.2313983

Another option to increase the amount of information is to employ frequency or time domain (TD) measurements [6], [7]. TD measurements have traditionally been the preferred experimental method for better resolving scattering and absorption and to obtain higher spatial resolution. TD measurements provide a larger amount of information than continuous wave (CW) or frequency domain (FD) measurements unless several frequencies are used. On the other hand, FD measurements usually include more photons in the statistics, which increases the signal-to-noise ratio (SNR), as the main source of noise is shot noise.

The photodetectors required for TD systems must have picosecond time resolution, while the evaluation of photon time-of-arrival is generally implemented with discrete time-to-digital converters (TDCs) that are often bulky and difficult to scale. In addition, converting the inverse problem from an underdetermined problem to a determined one requires a massive amount of data available for the image reconstruction. For this reason, researchers have employed large CCD cameras in NIRI with a variety of illumination systems [8]–[11]. However, CCDs do not usually have high time resolutions, and are not suited for ultra-fast and continuous operation.

The integration of single-photon avalanche diode (SPAD) detectors in CMOS technology [12] made it possible to detect single photons in compact and scalable sensors, thus paving the way to massively parallel photon counting image sensors. In particular, the integration of SPADs with TDCs in the same chip made it possible to perform simultaneous time-resolved measurements with a very large number of detectors [13]. This was so far impossible in conventional image sensors.

CW systems based on CCD cameras, although producing large datasets, lack information on photon's time of arrival. Moreover, as previously mentioned, time-resolved measurements provide higher resolution of scattering and absorbing objects, as well as higher depth sensitivity. Thus, SPAD image sensors fill the gap between these two approaches, bringing the best of both worlds to NIRI.

The aim of this paper is to present a NIRI setup based on a SPAD image sensor with 16 384 detectors, each capable of providing independent timing information [14]–[16] with picosecond resolution. We also systematically analyze the benefits and limitations of current SPAD image sensors when operating in time-correlated single photon counting (TCSPC) regime with an emphasis in NIRI applications. The paper is organized as follows, Section II presents the architecture of the setup. Section III outlines the proposed reconstruction algorithm. Section IV presents the results of the experimentation and Section V discusses the results giving a perspective for future sensors. Section VI concludes the paper.

II. SETUP

A. SPAD Image Sensor

The SPAD image sensor integrated in the NIRI setup was, to our knowledge, the first SPAD array that integrated on-chip TDCs [13]. It consists of a SPAD array of 128×128 SPAD pixels connected to a bank of 32 TDCs. The pixel's active area fill-factor is 6%. The TDCs have a time resolution of 97 ps

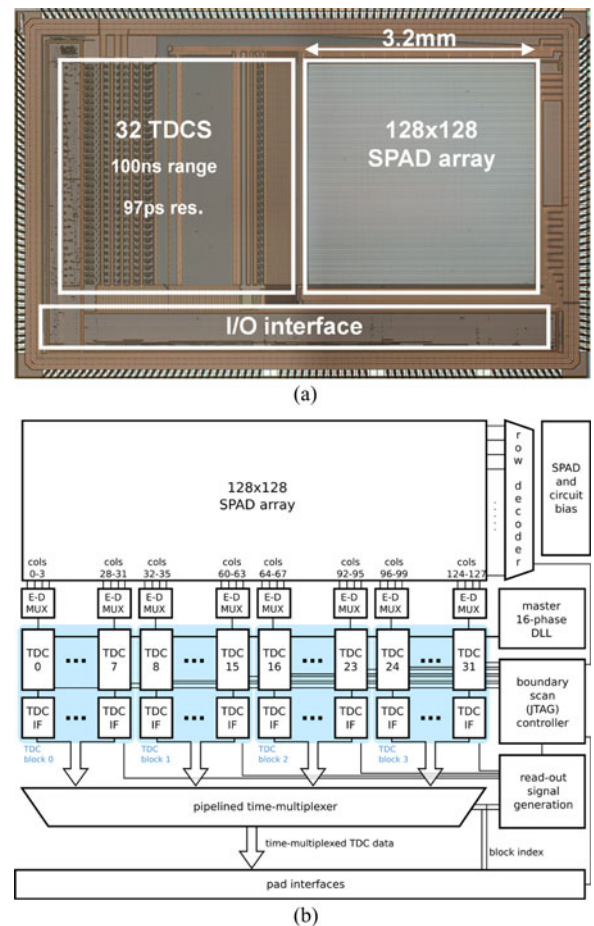


Fig. 2. (a) Microphotograph of the SPAD image sensor. It was fabricated in a standard CMOS HV $0.35 \mu\text{m}$ process. The dimensions of the active area are $3.2 \times 3.2 \text{ mm}^2$. (b) Block diagram of the SPAD image sensor.

and a range of 100 ns. When a row of pixels is selected, a direct connection between those pixels and the TDCs' bank is established. The pixels in a row are then divided in groups of four SPADs that are connected to a TDC using an event-driven mechanism. Consequently the sensor is capable of providing time resolved measurements for each of its pixels independently, making it suitable for TCSPC measurements. Fig. 2 shows a microphotograph of the chip and a schematic of the sensor's architecture.

Since only one row can be selected at any time, the readout of all rows requires a relatively long acquisition time. This is a drawback, because the ultimate aim is to perform measurements on human subjects in, or close to, real time to avoid artifacts from physiological changes and from the motion of the subject. Recently, SPAD image sensors have integrated TDCs in-pixel [17], i.e. all pixels in the sensor may simultaneously perform time-resolved measurements. However, this has resulted in pixels with a very low fill-factor, typically $\sim 1\%$, which is impractical for NIRI.

B. Optical Setup

NIRI systems can be classified into two types depending on the position of its sources and detectors. In transmission

mode, the subject under study is illuminated from one side and the backscattered light is measured at its opposite side. This approach restricts the range of objects that can be studied, because for objects thicker than 6 cm almost no light will reach the detectors. For this reason we decided to implement a NIRI setup in reflection mode where sources and detectors are placed on the same side of the object. This reflection approach enables the study of a wider range of tissues, and it is therefore clinically more relevant, however it limits the depth sensitivity to ~ 3 cm. The light backscattered close to the sources has a very fast response that cannot accurately be measured by TCSPC in our SPAD image sensor. Therefore a sufficient distance between sources and detectors is necessary. To measure backscattered light at very short source-detector distances requires dedicated discrete SPADs [18], [19].

Fast reconstruction algorithms published so far [11], [20] require placing the light sources inside the field of view of the camera when working in reflection mode, which is not possible as mentioned previously for our SPAD sensor. Therefore a new illumination system was conceived that reduces the complexity of the reconstruction algorithm, as explained in the next section, while taking the time information provided by the SPAD image sensor into consideration. The solution was to illuminate the object with parallel lines outside the field of view of the camera.

Fig. 3(a) shows the schematic of the NIRI setup and Fig. 3(b) a picture of its implementation. The light source is a 780 nm, 10 mW laser (Becker&Hickl BHL700). The repetition rate of the laser was 80 MHz, and it was set to deliver an average output power of 3 mW in order to keep the laser's time point spread function much faster than the measured signals. The lines are generated by a collimator and a line diffuser; a telecentric objective lens with a magnification factor $\beta = 0.07$, projects the backscattered light at the surface of the intralipid phantom to the SPAD image sensor. For each line source an acquisition is performed. Fig. 3(c) shows the typical response obtained in time resolved NIRI measurements. The pulse shape is captured by TCSPC as a reconstructed time histogram and its shape is determined by the absorption and scattering properties of the medium.

Intralipid phantoms with similar absorption and scattering properties as human tissue are produced for the experiments. These phantoms generally consist of a tank filled with a liquid composed of distilled water, intralipid emulsion, and Indian ink. These components can be mixed in different proportions to adjust the absorption and scattering coefficients. In this liquid we immersed the targets of the reconstructions. They were small objects made of silicon, carbon powder, and TiO_2 . Although in principle it is possible to resolve scattering and absorption of these targets, in this paper we only focused on absorbing targets, because they are clinically more relevant.

The theoretical framework described in the next section only takes into account changes in the absorption coefficient, but could be further developed for absorption and scattering changes. For this reason the targets and the intralipid phantom have the same scattering coefficient and only the absorption coefficient is varied in the targets in our experiments.

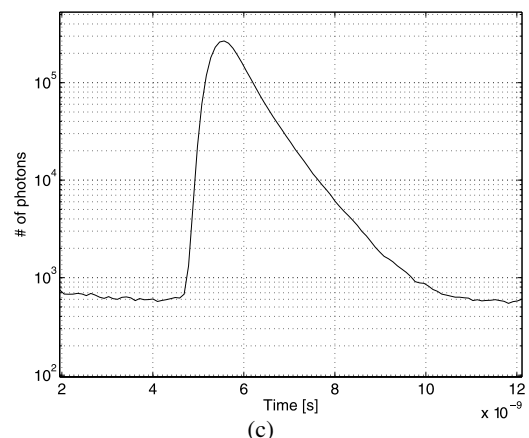
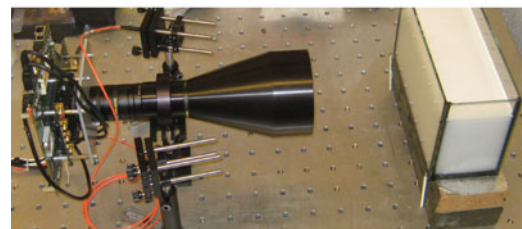
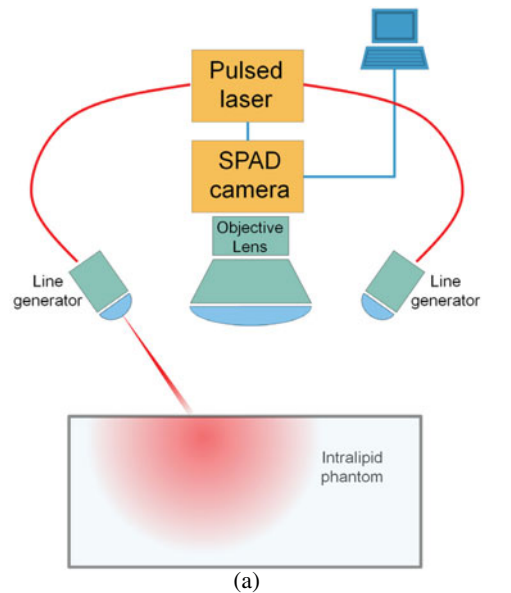


Fig. 3. (a) Schematic of the optical setup. A picosecond laser generates pulses of light that are projected as lines on the surface of the object under study. The light propagates through the object (diffusion process) and light emerging from the surface is captured by the objective lens and projected onto the SPAD sensor. Data is digitized in the camera and transferred to a computer. (b) Picture of the actual setup in the lab. (c) Response measured in an intralipid phantom with $\mu_a(\mathbf{r}) = 0.07 \text{ cm}^{-1}$ and $\mu'_s(\mathbf{r}) = 5 \text{ cm}^{-1}$ at a source-detector separation of 2 cm.

III. RECONSTRUCTION ALGORITHM

A. Theory

The reconstruction algorithm is based on the well-known diffusion equation [1], [14]. When a highly scattering medium, with given absorption $\mu_a(\mathbf{r})$ and reduced scattering $\mu'_s(\mathbf{r})$ coefficients, where $(\mu'_s(\mathbf{r}) \gg \mu_a(\mathbf{r}))$, is excited by a source

$q(\mathbf{r}, \mathbf{r}_s, \omega_t)$, positioned at \mathbf{r}_s with a temporal modulation frequency ω_t , the photon density in the medium $u(\mathbf{r}, \mathbf{r}_s, \omega_t)$ is governed by

$$\nabla^2 u(\mathbf{r}, \mathbf{r}_s, \omega_t) + k(\mathbf{r}, \omega_t)^2 u(\mathbf{r}, \mathbf{r}_s, \omega_t) = -q(\mathbf{r}, \mathbf{r}_s, \omega_t) / D(\mathbf{r}) \quad (1)$$

where

$$D(\mathbf{r}) = v / (3\mu'_s(\mathbf{r})) \quad (2)$$

$$k(\mathbf{r}, \omega_t)^2 = (-v\mu_a(\mathbf{r}) + i\omega_t) / D(\mathbf{r}) \quad (3)$$

and v is the speed of light in the medium. If the source term is an infinite line in the x -axis direction $q(\mathbf{r}, \mathbf{r}_s, \omega_t) = A(\omega_t) \delta(y - y_s, z - z_s)$ where $A(\omega_t)$ is the amplitude at a given ω_t frequency. The solution of (1) in a spatially homogeneous infinite medium where $\mu_a(\mathbf{r}) = \mu_a^{(0)}$ and $\mu'_s(\mathbf{r}) = \mu_s^{(0)}$, and therefore $k(\mathbf{r}, \omega_t) = k_0(\omega_t)$, is

$$u(\boldsymbol{\rho}, \boldsymbol{\rho}_s, \omega_t) = iH_0^{(1)}(k_0(\omega_t) |\boldsymbol{\rho} - \boldsymbol{\rho}_s|) / (4D) \quad (4)$$

where $H_0^{(1)}$ is a Hankel function of the first kind, $\boldsymbol{\rho} = (y, z)$, and $\boldsymbol{\rho}_s = (y_s, z_s)$ is the position of the line source term.

In order to calculate $u(\mathbf{r}, \omega_t)$ when the medium is not homogeneous in terms of the absorption coefficient we decompose $\mu_a(\mathbf{r}) = \mu_a^{(0)} + \delta\mu_a(\mathbf{r})$ and $u(\mathbf{r}, \mathbf{r}_s, \omega_t) = u_0(\mathbf{r}, \mathbf{r}_s, \omega_t) + u_s(\mathbf{r}, \mathbf{r}_s, \omega_t)$ where $u_0(\mathbf{r}, \omega_t)$ is the photon density in a homogeneous medium with absorption coefficient $\mu_a^{(0)}$. If the medium is illuminated by line shaped light sources, then $u_0(\mathbf{r}, \mathbf{r}_s, \omega_t)$ will equal (4). Substituting these terms in (1) results in

$$(\nabla^2 + k_0(\omega_t)^2)u_s(\mathbf{r}, \mathbf{r}_s, \omega_t) = \delta\mu_a(\mathbf{r})u(\mathbf{r}, \mathbf{r}_s, \omega_t) v / D. \quad (5)$$

If we assume that $u_0(\mathbf{r}, \mathbf{r}_s, \omega_t) \gg u_s(\mathbf{r}, \mathbf{r}_s, \omega_t)$ then (5) can be expressed as

$$(\nabla^2 + k_0(\omega_t)^2)u_s(\mathbf{r}, \mathbf{r}_s, \omega_t) = \delta\mu_a(\mathbf{r})u_0(\mathbf{r}, \mathbf{r}_s, \omega_t) v / D. \quad (6)$$

This simplification step is commonly known as the first Born approximation. Now (5) can be solved in terms of the equation's Green's function

$$u_s(\mathbf{r}, \mathbf{r}_s, \omega_t) = -\iiint g(\mathbf{r}|\mathbf{r}', \omega_t) \delta\mu_a(\mathbf{r}) u_0(\mathbf{r}', \mathbf{r}_s, \omega_t) v / D d^3\mathbf{r}' \quad (7)$$

where $g(\mathbf{r}|\mathbf{r}', \omega_t)$ is the Green's function of (5). Equation (7) served as the basis for many reconstruction algorithms in previous studies [5]. It is essentially a linearized version of (6) among others such as the Rytov approximation. The idea behind these reconstruction algorithms is that it is possible to recover $\delta\mu_a(\mathbf{r})$ from a finite number of boundary measurements of $u_s(\mathbf{r}, \mathbf{r}_s, \omega_t)$. Measurements of $u_s(\mathbf{r}, \mathbf{r}_s, \omega_t)$ at different locations of the boundary, generated by sources placed at different positions will create a collection of data to recover $\delta\mu_a(\mathbf{r})$. It is also possible to increase the amount of information available to calculate $\delta\mu_a(\mathbf{r})$ by employing light sources with different temporal modulation frequencies ω_t . With the acquired information, it is possible to discretize (7) and to invert the three-dimensional integral equation. In most of the cases the number of unknowns

defined by $\delta\mu_a(\mathbf{r})$ is much higher than the number of measurements $u_s(\mathbf{r}, \mathbf{r}_s, \omega_t)$, i.e. the problem is underdetermined and therefore without a unique solution. These types of problems are commonly known in physics as inverse problems. Their inversion is non-trivial and in many cases it requires some kind of regularization to obtain meaningful results. The aim is to generate a large dataset of measurements to achieve an integral equation that is not underdetermined anymore. In this case it is possible to generate a full rank system in which the system's matrix can be inverted independently of the measured data. The multiplication of this matrix by the measured data will generate a unique solution to the problem.

Due to the restrictions of the setup described in the first part, we decided to develop a new reconstruction algorithm that traded off computation power with the number of measurements required to obtain a reconstructed image. The starting point of the algorithm is (6), in the presence of line-like illumination, resulting in

$$(\nabla^2 + k_0(\omega_t)^2)u_s(\mathbf{r}, \mathbf{r}_s, \omega_t) = \delta\mu_a(\mathbf{r})u_0(\boldsymbol{\rho}, \boldsymbol{\rho}_s, \omega_t) v / D \quad (8)$$

where $u_0(\boldsymbol{\rho}, \boldsymbol{\rho}_s, \omega_t)$ is defined in (4). If we apply the Fourier transformation defined by

$$\tilde{u}(\boldsymbol{\rho}, \mathbf{q}, \omega_t) = \int u_s(\mathbf{r}, \omega_t) e^{-i\mathbf{q}\cdot\mathbf{r}} d\mathbf{r} \quad (9)$$

then (8) results in

$$(\nabla_{yz}^2 + \gamma(\mathbf{q}, \omega_t)^2)\tilde{u}_s(\boldsymbol{\rho}, \boldsymbol{\rho}_s, \mathbf{q}, \omega_t) = \delta\tilde{\mu}_a(\boldsymbol{\rho}, \mathbf{q})u_0(\boldsymbol{\rho}, \boldsymbol{\rho}_s, \omega_t) v / D \quad (10)$$

where $\gamma(\mathbf{q}, \omega_t)^2 = -q^2 + k_0(\omega_t)^2$. The solution of (10) in an infinite medium has the following integral expression

$$\begin{aligned} u_s(\boldsymbol{\rho}, \boldsymbol{\rho}_s, \mathbf{q}, \omega_t) &= -\iint g(\boldsymbol{\rho}|\boldsymbol{\rho}', \mathbf{q}, \omega_t) \delta\tilde{\mu}_a(\boldsymbol{\rho}', \mathbf{q}) u_0(\boldsymbol{\rho}', \boldsymbol{\rho}_s, \omega_t) v / D d^2\boldsymbol{\rho}' \\ &= -\iint g(\boldsymbol{\rho}|\boldsymbol{\rho}', \mathbf{q}, \omega_t) \delta\tilde{\mu}_a(\boldsymbol{\rho}', \mathbf{q}) u_0(\boldsymbol{\rho}', \boldsymbol{\rho}_s, \omega_t) v / D d^2\boldsymbol{\rho}' \end{aligned} \quad (11)$$

where

$$g(\boldsymbol{\rho}|\boldsymbol{\rho}', \mathbf{q}, \omega_t) = iH_0^{(1)}(\gamma(\mathbf{q}, \omega_t) |\boldsymbol{\rho} - \boldsymbol{\rho}'|) / 4 \quad (12)$$

is the Green's function of (10) in an infinite medium. Equation (11) can be independently inverted for each \mathbf{q} component. When $\delta\tilde{\mu}_a(\boldsymbol{\rho}, \mathbf{q})$ is calculated for a range of equidistant \mathbf{q} it is possible to apply the Fourier inversion operator to calculate $\delta\mu_a(\mathbf{r})$. The advantage of (11) with respect to (7) lies in the computational complexity of the inversion problem. Since in (11) the integral equation is only two dimensional, although many more equations need to be inverted, the computational power required to reconstruct $\delta\mu_a(\mathbf{r})$ is much lower than that for the three dimensional equation in (7). As an example, we compare the computational complexity necessary to calculate $\delta\mu_a(\mathbf{r})$ when singular value decomposition is used to invert the integral equations. In an infinite medium with $N \times N \times N$ voxels, measurements are acquired at $N \times P$ points at Q different modulation frequencies. The computational complexity of a reconstruction algorithm based on (7) then is $O((N \times P \times Q)^2 \times N \times N \times N)$ whereas

for (11) it is $O(((P \times Q)^2 + \log N) \times N \times N \times N)$. Not only is the complexity considerably reduced, but the algorithm based on (11) requires solving many independent inverse problems and could therefore easily be parallelized. An algorithm based on (7) would only have a single inverse problem, which would be very difficult to parallelize.

The proposed algorithm has been formulated for an infinite medium, but it could be applied to any medium that was infinite in at least one spatial direction. It has been recently suggested that boundary removal techniques [21] could be applied in fast reconstruction algorithms so they can work with media with arbitrary geometries [5]. As previously mentioned, although in this paper the target of the reconstructions were only absorption changes in the medium, it is possible to expand the algorithm to simultaneously reconstruct changes in scattering and absorption [22].

B. Implementation

The implemented reconstruction algorithm was based on (11), where instead of using the Green's function for an infinite medium, the Green's function was calculated for a semi-infinite medium using extrapolated boundary conditions [23]. The main requirement for the algorithm was to work with a reduced number of rows of pixels and source positions to perform measurements in a short period of time. For each source position and pixel row a new acquisition needs to be performed. In the implementation of the algorithm presented in this contribution, only three rows of pixels and two source lines placed at opposite sides of the detector were necessary. With more sources and detectors it would be possible to increase the volume that can be reconstructed and the accuracy of the reconstructions would improve as well. However, since the ultimate goal is to perform measurements on human subjects the total acquisition time is a critical factor that needs to be kept as short as possible.

The data obtained from the detector is time-resolved, however the presented algorithm only works with frequency-domain data. Therefore a fast Fourier transform is required to convert the measured signals in frequency domain data. Since the time resolution of the TDC is 97 ps, the maximum modulation frequency is ~ 5 GHz.

Due to the ill-posed nature of the problem, the specific algorithm inverting (11) has a large impact on the quality of the reconstructions. Therefore, inversion algorithms require some type of regularization. In our implementation, the subspace preconditioned LSQR algorithm presented in [24] was chosen to solve the inversion problem due to its iterative nature and its Tikhonov regularization scheme [24].

IV. RESULTS

A. Simulations

We performed simulations to evaluate the performance of the reconstruction algorithm in the absence of noise. In order to assess the ideal resolution of our setup together with the algorithm, a testbench that mimicked the experimental setup was implemented. Fig. 4(a) shows a schematic of the setup

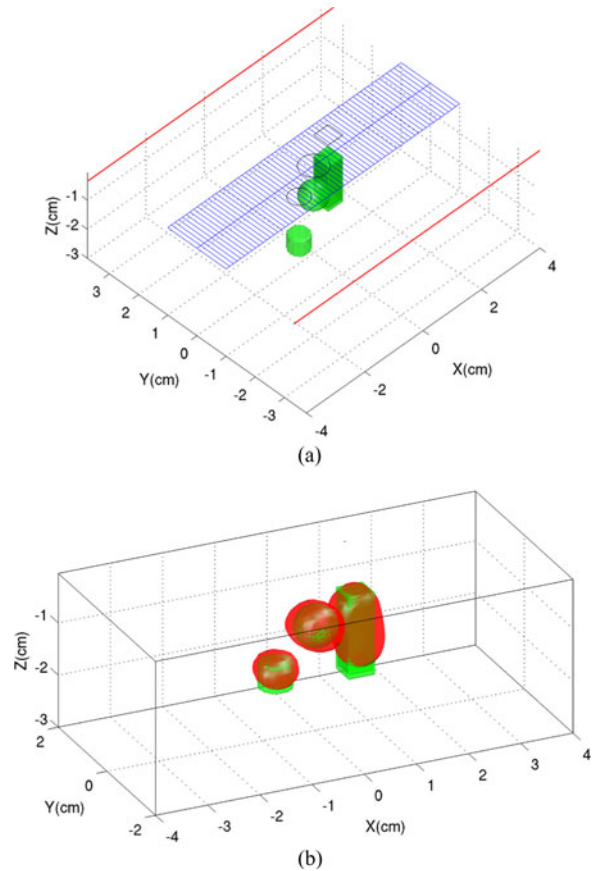


Fig. 4. (a) Three dimensional representation of the setup in the simulation testbench. In a semi-infinite medium three objects with higher absorption coefficients are placed at different positions. The XY plane at $z = 0$ is the boundary of the medium. Two infinite lines of light are projected on the boundary plane at $y = [-3.5, 3.5]$ to illuminate the medium. Three lines of 64 pixels located at $y = [-1, 0, 1]$ measure the backscattered light from the medium. (b) Reconstructed three dimensional images of the objects superimposed on top of the original targets.

where the sources, detectors, and objects with increased absorption coefficient are visible. In the testbench a semi-infinite medium with $\mu_a = 0.1 \text{ cm}^{-1}$ and $\mu'_s = 10 \text{ cm}^{-1}$ with three differently shaped objects with optical properties $\mu_a = 0.30 \text{ cm}^{-1}$ and $\mu'_s = 10 \text{ cm}^{-1}$ was modeled. This resulted in an absorption contrast ratio of 3, which is a moderate contrast in NIRI, e.g. the optical contrast between blood vessels and its surrounding tissue is usually two orders of magnitude higher.

Fig. 4(b) shows the targets and the corresponding reconstruction. As expected the edges of the objects are not well detected, however the position and shape of the reconstructions match the targets with high accuracy. The reconstruction of the long cube-shaped object is particularly remarkable since traditionally NIRI algorithms lack accurate depth resolution. In the cross-sections of Fig. 5 the high accuracy of the absorption coefficient is displayed. In the pictures it is visible that in certain areas negative absorption values are reconstructed. Although this is physically not possible, it often occurs in NIRI reconstructions when in the inversion step no restrictions are set on the sign of the solution. Reconstructions with $1.25 \text{ mm} \times 1.25 \text{ mm} \times 1.25 \text{ mm}$ voxels

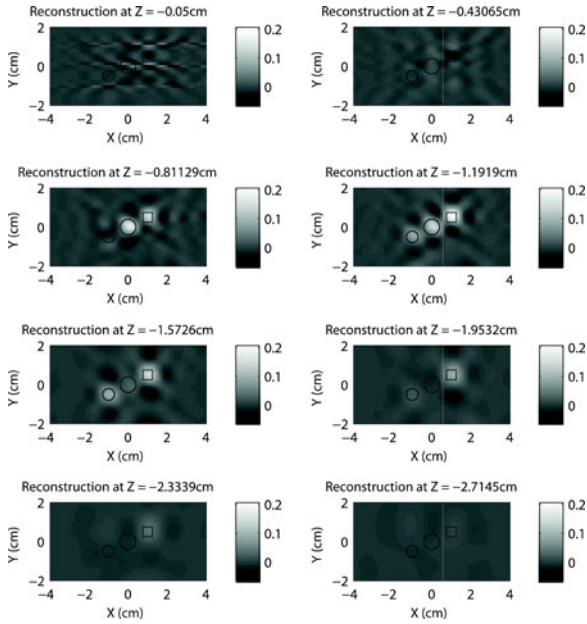


Fig. 5. Cross-sections of the reconstruction at different depths. The reconstructed differences in the value of the absorption coefficient to the background absorption are very close to the original ones of 0.2 cm^{-1} .

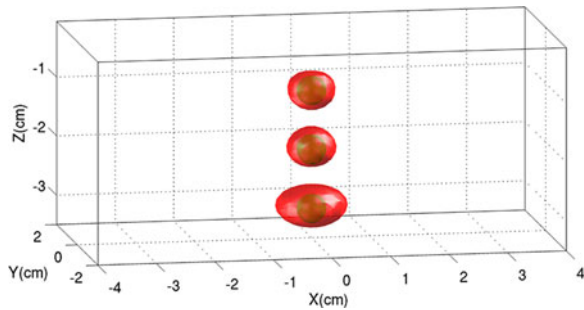


Fig. 6. Superimposition of the three reconstructions of a sphere placed at different depths of the phantom.

and 32 temporal modulation frequencies required ~ 20 s of CPU time on a desktop computer.

To assess the depth sensitivity of our algorithm a testbench with a single absorbing sphere placed at different depths was simulated. Fig. 6 shows the superimposed results from the three different simulations. These simulations showed much better results than previous time resolved NIRI algorithms based on the usage of discrete components [25].

B. Experimental Results

Experimental measurements were performed with an intralipid phantom with optical properties $\mu_a = 0.07 \text{ cm}^{-1}$ and $\mu'_s = 5 \text{ cm}^{-1}$ which contained two cylinders of 5 mm diameter separated by 5 mm placed at $z = -1 \text{ cm}$ with optical properties $\mu_a = 0.25 \text{ cm}^{-1}$ and $\mu'_s = 5 \text{ cm}^{-1}$. μ_a and μ'_s have been reduced compared to those employed in the simulation in order to increase the intensity of the measured light, consequently reducing the influence of noise, and to ensure that the measured signals had a much slower response than the system's impulse

response function (IRF). If the system's IRF was comparable or slower than the measured signals, then it would be necessary to deconvolve the measured signal with the system's IRF before performing any reconstruction. Trials with higher absorption and scattering showed poor results in terms of SNR indicating that the setup needs to be improved for higher absorbing or scattering media. The position of the sources and detectors was also modified to increase the SNR: the sources are in this case closer to the detectors to increase the intensity of the measured signal, and the distance between detectors has been reduced so that the difference of signal level among them is smaller. In the current setup the source lights are placed at $y = [-2.65, 2.65]$, whereas the detectors are placed at $y = [-0.6, 0, 0.6]$. In this case the 128 pixels in each row were binned into 32 detectors to improve the SNR. The acquisition time for each row of pixels was about 6 min. The power of the laser and the source-detector distances were adjusted so that the maximum detection rate in the pixels was never higher than 1% of $1/T_0$, where T_0 is the TDC's conversion period, which in this particular case was 100 ns. This was done in order to avoid pile-up effects in the histograms and to ensure that the pixels were always working in single-photon detection regime. In the reconstruction a voxel of size $0.94 \text{ mm} \times 1.44 \text{ mm} \times 1.25 \text{ mm}$ and 32 temporal modulation frequencies were employed. Fig. 7(a) shows the experimental setup and Fig. 7(b) the reconstructed image. Both cylinders are clearly resolved indicating that a resolution of at least 5 mm is achieved with the current setup and reconstruction algorithm.

The limited field of view of the setup (only three pixel rows placed at intervals of 6 mm were employed) naturally limited the volume in which the objects were reconstructed. This is the reason why the ends of the cylinders were not visible in the reconstructed image, since they were outside the field of view of the sensor.

Fig. 8 shows the cross section of the reconstruction at different depths. In these cross sections both cylinders are clearly differentiated reaching an absorption coefficient of $\sim 0.2 \text{ cm}^{-1}$, which is close to the real absorption coefficient of the target cylinders.

V. DISCUSSION AND PERSPECTIVES

The possibility of performing high-resolution time resolved measurements with SPAD image sensors opened a new era in many biomedical and biological imaging fields [26]. Their suitability for NIRI has been probed in this paper, enabling for the first time NIRI devices with high spatial resolution and time resolved measurements.

There are certain limitations in actual SPAD image sensors that could have a large impact in the performance of NIRI devices if they were addressed. The relatively small field of view of the presented system was limited by the size of the sensor's active area ($3.2 \text{ mm} \times 3.2 \text{ mm}$). Although sensors with larger active areas have been developed [17], they are still small in comparison to commercial CCD and CMOS sensors. So far most SPAD pixels integrated in image sensors exhibit low fill-factors, making them inefficient in low light applications like NIRI. Although we recently showed how microlenses can

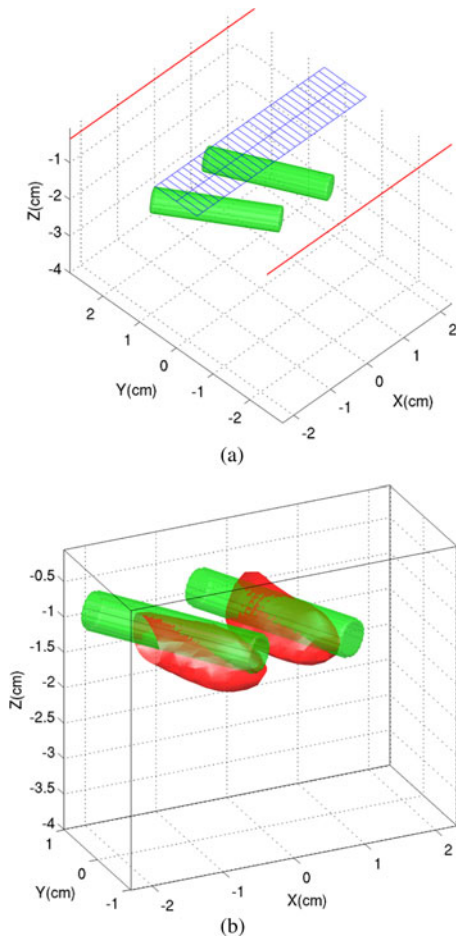


Fig. 7. (a) Representation of the intralipid phantom with the two cylinders in it. The XY plane at $z = 0$ represents the wall of the tank on which the light is projected and where the backscattered photons are measured. (b) Reconstructed three-dimensional images of the objects superimposed on top of the original targets.

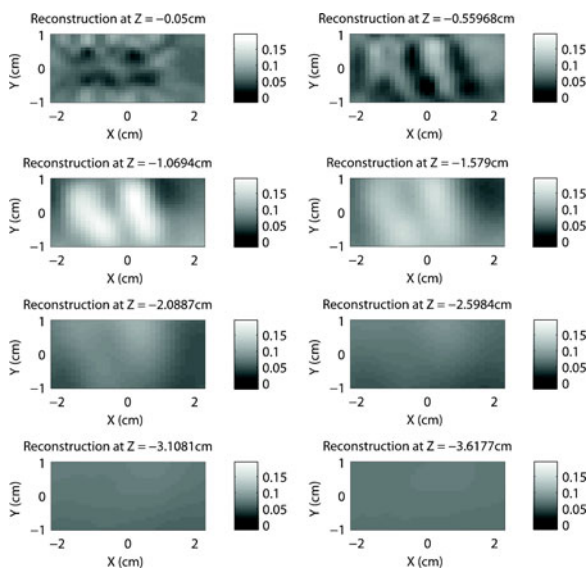


Fig. 8. Cross-sections of the reconstruction at different depths. The reconstructed absorption values are lower than the targets' ones. However, the integral of the absorption coefficient in the reconstructed objects should be similar to the integral of the absorption coefficient in the target objects.

improve the fill-factor in SPAD image sensors [27], their performance strongly depends on the optical system where they are integrated. In particular the image sensor that was employed in the presented experiments did not have microlenses. Nevertheless there have been recent advances in the development of SPAD pixels [28], showing that it is possible to reach fill-factors similar to those in commercial CMOS sensors by implementing square SPADs with rounded corners.

At the moment the most critical factor for SPAD image sensors when applied in *in-vivo* biomedical application is the measurement time. Most sensors architectures are based on sequential reading of the pixels similar to those used in CMOS sensors. However due to the low activity rate of the pixels in time resolved measurements it is necessary to read every pixel for long periods of time to obtain enough statistics of the photons. Event-driven approaches similar to the ones implemented in digital SiPMs [28], in which concurrent reading of the pixels is possible will drastically reduce the measurement time with SPADs sensors making them suitable for *in-vivo* measurements.

VI. CONCLUSION

In this contribution it has been demonstrated how NIRI can benefit from high accuracy time-resolved measurements offered by SPAD image sensors. Reconstructed images with millimetric resolution were obtained with a SPAD image sensor prototype. NIRI will benefit in the coming years from the new advances that are undergoing in this still young technology.

We believe that high resolution NIRI systems with fast acquisition times can open a new dimension in clinical applications, by enabling the measurement of oxygenation state of organs, e.g. the brain, muscle, liver among others, in real time and with sub-centimeter resolution.

REFERENCES

- [1] M. A. O'Leary, "Imaging with diffuse photon density waves," Ph.D. dissertation, Dept. Phys. Astro., Univ. Penn., Philadelphia, PA, USA, 1996.
- [2] S. R. Arridge, M. Schweiger, M. Hiraoka, and D. T. Delpy, "A finite element approach for modeling photon transport in tissue," *Med. Phys.*, vol. 20, no. 2, pp. 299–309, Apr. 1999.
- [3] H. Dehghani, M. E. Eames, P. K. Yalavarthy, S. C. Davis, S. Srinivasan, C. M. Carpenter, B. W. Pogue, and K. D. Paulsen, "Near infrared optical tomography using NIRFAST: Algorithm for numerical model and image reconstruction," *Commun. Numer. Methods Eng.*, vol. 25, no. 6, pp. 711–732, Aug. 2008.
- [4] Q. Fang and D. A. Boas, "Monte carlo simulation of photon migration in 3D turbid media accelerated by graphics processing units," *Opt. Exp.*, vol. 17, no. 22, pp. 20178–20190, Oct. 2009.
- [5] S. R. Arridge and J. C. Schotland, "Optical tomography: Forward and inverse problems," *Inverse Prob.*, vol. 5, no. 12, Dec. 2009.
- [6] S. Fantini, M.-A. Franceschini, J. S. Maier, S. A. Walker, B. B. Barbieri, and E. Gratton, "Frequency-domain multichannel optical detector for non-invasive tissue spectroscopy and oximetry," *Opt. Engr.*, vol. 34, no. 1, pp. 32–42, Jan. 1995.
- [7] M. S. Patterson, B. Chance, and B. C. Wilson, "Time resolved reflectance and transmittance for the non-invasive measurement of tissue optical properties," *Appl. Opt.*, vol. 28, no. 12, pp. 2331–2336, Jun. 1989.
- [8] V. A. Markel and J. C. Schotland, "Inverse problem in optical diffusion tomography. I. fourier-laplace inversion formulas," *J. Opt. Soc. Am. A*, vol. 18, no. 6, pp. 1336–1347, Jun. 2001.
- [9] D. Abookasis, C. C. Lay, M. S. Mathews, M. E. Linskey, R. D. Frostig, and B. J. Tromberg, "Imaging cortical absorption, scattering, and hemodynamic response during ischemic stroke using spatially modulated

- near-infrared illumination," *J. Biomed. Opt.*, vol. 14, no. 2, p. 024033, Apr. 2009.
- [10] S. D. Konecky, A. Mazhar, D. Cuccia, A. J. Durkin, J. Schotland, and B. J. Tromberg, "Quantitative optical tomography of sub-surface heterogeneities using spatially modulated structured light," *Opt. Expr.*, vol. 17, no. 17, pp. 14780–14790, Aug. 2009.
- [11] S. D. Konecky, G. Y. Panasyuk, K. Lee, V. Markel, A. G. Yodh, and J. C. Schotland, "Imaging complex structures with diffuse light," *Opt. Expr.*, vol. 16, no. 7, pp. 5048–5060, Mar. 2008.
- [12] A. Rochas, M. Gani, B. Furrer, P. A. Besse, R. S. Popovic, G. Ribordy, and N. Gisin, "Single photon detector fabricated in a complementary metal-oxide-semiconductor high-voltage technology," *Rev. Sci. Instr.*, vol. 74, no. 7, pp. 3263–3270, Jul. 2003.
- [13] C. Niclass, C. Favi, T. Kluter, M. Gersbach, and E. Charbon, "A 128 × 128 single-photon image sensor with column-level 10-bit time-to-digital converter array," *IEEE J. Solid-State Circuits*, vol. 43, no. 12, pp. 2977–2989, Dec. 2008.
- [14] J. Mata Pavia, E. Charbon, and M. Wolf, "3D near-infrared imaging based on a single-photon avalanche diode array sensor," in *Proc. SPIE Diffuse Opt. Imag.*, III, vol. 8099, no. 1, Munich, Germany, Jun. 2011.
- [15] J. Mata Pavia, E. Charbon, and M. Wolf, "3D near-infrared imaging based on a single-photon avalanche diode array sensor," presented at the SPIE Biosensing Nanomedicine V, San Diego, CA, USA, vol. 84601, Oct. 2012.
- [16] J. Mata Pavia, E. Charbon, and M. Wolf, "3D near-infrared imaging based on a single-photon avalanche diode array sensor: A new perspective on reconstruction algorithms," presented at the OSA Tech. Dig. Biomed. Opt. 3D Imag., Miami, FL, USA, May 2012, p. BW1A.5.
- [17] C. Veerappan, J. Richardson, R. Walker, Day-Uey Li, M. W. Fishburn, Y. Maruyama, D. Stoppa, F. Borghetti, M. Gersbach, R. K. Henderson, and E. Charbon, "A 160 × 128 single-photon image sensor with on-pixel 55ps 10b time-to-digital converter," in *Proc. Tech. Dig. IEEE Int. Solid-State Circ. Conf.*, Feb. 2011, pp. 312–314, vol. 20–24.
- [18] A. Dalla Mora, D. Contini, A. Pifferi, R. Cubeddu, A. Tosi, and F. Zappa, "Afterpulse-like noise limits dynamic range in time-gated applications of thin-junction silicon single-photon avalanche diode," *Appl. Phys. Lett.*, vol. 100, no. 24, pp. 241111–241114, Jun. 2012.
- [19] A. Pifferi, A. Torricelli, L. Spinelli, D. Contini, R. Cubeddu, F. Martelli, G. Zaccanti, A. Tosi, A. Dalla Mora, F. Zappa, and S. Cova, "Time-resolved diffuse reflectance using small source-detector separation and fast single-photon gating," *Phys. Rev. Lett.*, vol. 100, no. 13, pp. 138101–138104, Mar. 2008.
- [20] V. Lukic, V. A. Markel, and J. C. Schotland, "Optical tomography with structured illumination," *Opt. Lett.*, vol. 34, no. 7, pp. 983–985, Apr. 2009.
- [21] J. Ripoll and V. Ntziachristos, "From finite to infinite volumes: Removal of boundaries in diffuse wave imaging," *Phys. Rev. Lett.*, vol. 96, no. 17, pp. 173903–173904, May 2006.
- [22] V. A. Markel and J. C. Schotland, "Symmetries, inversion formulas and image reconstruction for optical tomography," *Phys. Rev. E*, vol. 70, no. 5, pp. 056616–056619, Nov. 2004.
- [23] R. Haskell, L. Svaasand, T. Tsay, T. Feng, M. McAdams, and B. Tromberg, "Boundary conditions for the diffusion equation in radiative transfer," *J. Opt. Soc. Am. A*, vol. 11, no. 10, pp. 2727–2741, Oct. 1994.
- [24] M. Jacobsen, P. C. Hansen, and M. A. Saunders, "Subspace preconditioned LSQR for discrete ill-posed problems," *BIT Num. Math.*, vol. 43, no. 5, pp. 975–989, Dec. 2003.
- [25] J. Selb, A. M. Dale, and D. A. Boas, "Linear 3D reconstruction of time-domain diffuse optical imaging differential data: improved depth localization and lateral resolution," *Opt. Expr.*, vol. 15, no. 25, pp. 16400–16412, Dec. 2007.
- [26] E. Charbon and S. Donati, "SPAD sensors come of age," *Opt. Phot. News*, vol. 21, no. 2, pp. 34–41, Feb. 2010.
- [27] J. Mata Pavia, M. Wolf, and E. Charbon, "Measurement and modeling of microlenses fabricated on single-photon avalanche diode arrays for fill factor recovery," *Opt. Expr.*, vol. 22, no. 4, pp. 4202–4213, Feb. 2014.
- [28] S. Mandai and E. Charbon, "A 4 × 4 × 416 digital SiPM array with 192 TDCs for multiple high-resolution timestamp acquisition," *J. Instr.*, vol. 8, no. 5, p. P05024, May 2013.

Juan Mata Pavia received the M.S. degree in electrical engineering from the Royal Institute of Technology, Stockholm, Sweden, and the telecommunications engineering Diploma degree from the Polytechnic University of Valencia, Valencia, Spain, both in 2004. In 2009, he joined the Swiss Federal Institute of Technology Lausanne, Lausanne, Switzerland, where he is currently working toward the Ph.D. degree at the Quantum Architecture Group. After his graduation, he joined Philips Semiconductors, Eindhoven, The Netherlands, where he was involved in the design of application processors for smartphones. He is currently working at the University Hospital Zurich, Zurich, Switzerland, investigating the design of new single-photon detectors for biomedical imaging applications.



Martin Wolf received the M.S. degree in electrical engineering from the Swiss Federal Institute of Technology (ETH), Zurich, Switzerland, in 1990. His focus was on biomedical and power engineering. He received the Ph.D. degree from ETH, in 1997, where he specialized in biomedical optics, i.e., near-infrared spectroscopy to investigate tissue oxygenation. As a Postdoctoral Research Associate, he worked at the Division for Neonatology, University Hospital Zurich, Zurich, until 1999, when he joined the Laboratory for Fluorescence Dynamics at the University

of Illinois at Urbana-Champaign, Urbana-Champaign, IL, USA. He developed imaging methods to noninvasively study hemodynamics and oxygenation of the brain and muscle. Since 2002, he heads the Biomedical Optics Research Laboratory at the Division of Neonatology, University Hospital Zurich, where he currently expands the research in biomedical optics to many clinical fields. In 2004, he became Lecturer, and in 2013, a Professor at the University Zurich, Zurich.



Edoardo Charbon (SM'00) received the Diploma degree from the Swiss Federal Institute of Technology Zurich, Zurich, Switzerland, the M.S. degree from the University of California at San Diego, San Diego, CA, USA, and the Ph.D. degree from the University of California at Berkeley, Berkeley, CA, in 1988, 1991, and 1995, respectively, all in electrical engineering and electrical engineering and computer science. He is currently a Consultant for numerous organizations, including Bosch, Texas Instruments, Agilent, and the Carlyle Group. He was with Cadence

Design Systems, from 1995 to 2000, where he was an Architect of the company's initiative on information hiding for intellectual property protection. In 2000, he joined Canesta Inc., as the Chief Architect, where he led the development of wireless 3-D CMOS image sensors. From 2002 to 2008, he was a Faculty Member with the École Polytechnique Fédérale de Lausanne, Lausanne, Switzerland, where he was involved in research on CMOS sensors, biophotonics, and ultra low-power wireless embedded systems. In 2008, he joined Delft University of Technology, Delft, The Netherlands, as a Full Professor of VLSI design, succeeding Patrick Dewilde. He has authored or co-authored over 250 papers in journals, conference proceedings, magazines, and two books, and he holds 15 patents. His current research interests include 3-D imaging, advanced biomedical imaging, quantum integrated circuits, and space-based detection. Dr. Charbon was a Guest Editor of the IEEE TRANSACTIONS ON COMPUTER-AIDED DESIGN OF INTEGRATED CIRCUITS AND SYSTEMS and the IEEE JOURNAL OF SOLID STATE CIRCUITS and a Member of the Chair of Technical Committee of ESSCIRC, ICECS, ISLPED, VLSI-SOC, and IEDM. He is a Distinguished Visiting Scholar with the W. M. Keck Institute for Space, California Institute of Technology, Pasadena, CA.